First-principles study on secondary electron emission of MgO surface

Youngmi Cho and Changwook Kim
CAE Team, Samsung SDI, Co., Ltd., Yongin 446-557, Korea

Hyo-Shin Ahn
Center for Strongly Correlated Materials Research, Seoul National University, Seoul 151-747, Korea

Eunae Cho, Tae-Eun Kim, and Seungwu Han[a)]
Department of Physics, Ewha Womans University, Seoul 120-750, Korea

(Received 24 January 2007; accepted 27 February 2007; published online 30 April 2007)

We theoretically investigate secondary-electron-emission properties of MgO when noble gases are incident on the surface. We consider both potential and kinetic emission mechanisms. For the potential emission through Auger neutralization, densities of states and vacuum level are obtained from the first-principles calculations. It is found that secondary-emission coefficients decrease in the following sequence of surface directions; (111)-OH > (100) > (110), a tendency that is in agreement with experimental observations. For a surface model including *F* center, the secondary-emission coefficient substantially increases for Kr and Xe. To investigate the kinetic emission mechanism by an energetic ion impinging on MgO surfaces, first-principles molecular dynamics simulations are performed. Dynamic up-shifts of antibonding states between ions and oxygen atoms are found to lead to the secondary-electron emission at kinetic energies as low as 30 eV. Various collision conditions are compared based on the temporal interval during which excited states stay within the conduction band. © *2007 American Institute of Physics*. [DOI: 10.1063/1.2721857]

I. INTRODUCTION

As the size of discharge cells in a plasma display cell (PDP) is reduced toward the production of high-definition television, the luminescence of each cell has become a main issue.[1] To improve the luminescence efficiency, cell structures, gas compositions, and driving waveforms have been optimized. Recently, it has been realized that the luminescence efficiency, as well as the overall lifetime or stability of the device, are significantly influenced by the protective layer.[2] There are several material properties required for an ideal protective layer: large secondary-electron-emission (SEE) coefficients, low sputtering rates, and good transparency. Among the materials satisfying these conditions,[3,4] MgO was most widely used until now. Owing to the high SEE coefficients, MgO layers play an important role in lowering the firing voltage, which is directly related to the power consumption of the cell.[5]

In spite of its paramount importance, the relationship between material properties of thin MgO layer and discharge performance are barely revealed.[6,7] For example, many studies reported dependence of SEE coefficients of MgO on the growth direction but the microscopic origin is yet to be understood.[5,8] Such a lack of information is now posing a barrier to optimize the discharge cell through materials engineering. To understand the complicated surface-ion interaction between the discharge gas and MgO surface, theoretical analysis is required in parallel with extensive experimental measurements. In fact, the surface charging on insulators prohibits precise measurements of SEE coefficients. The quantum-mechanical nature of SEE processes indicates that first-principles modeling could be a very useful tool for understanding SEE phenomena. However, there are few theoretical attempts to study material properties of MgO in view of its functions in PDP discharge cell.[9] Motivated by these situations, we employ in this work first-principles approaches to study SEE phenomena of MgO.

The emission mechanism of secondary electrons from MgO surface can be divided according to the source of stimulation, origin of emitted electrons, and physical/chemical processes of the emission.[10] In the present work, we mainly discuss the SEE mechanisms associated with surface-ion interactions, which have been known as dominant mechanisms in the cell of PDP during operation. We specifically focus on two processes leading to SEE; potential and kinetic emissions. In the case of the potential emission mechanism,[3,11] electrons are emitted through the Auger process and the energy transfer occurs via neutralization of ions. On the other hand, the transfer of kinetic energy of incoming ions to the electrons bound at surface leads to the emission in the kinetic mechanism.[12] This paper is organized as follows: in Sec. II, we will discuss the potential and kinetic emission mechanisms in more detail. The computational setup will be presented in Sec. III. Computational results and discussions are given in Sec. IV. Section V summarizes main results.

II. THEORETICAL BACKGROUND

A. Potential emission mechanism

The potential emission is the major source of the secondary electron emission by the ionized particles. In this mechanism, electrons are emitted to the vacuum through the Auger process, which is stimulated by the energy conversion that

[a)]Author to whom correspondence should be addressed; electronic mail: hansw@ewha.ac.kr

occurs when the incoming ions are neutralized by electrons bound at the MgO surface.[3,11] There are two experimental observations that are consistent with the potential emission: (i) The SEE coefficient increases with the ionization energy of the incoming ion. (ii) The kinetic energy of the emitted electrons depends on the electronic properties of the surface such as energy gaps and electron affinities. These characteristics are represented by Eq. (1):[3]

$$E_K^{\max} = E_i - 2(E_g + \chi), \tag{1}$$

where $E_K^{\max}$ is the maximum kinetic energy of the secondary electron, E_i is the ionization energy of the incoming ion, and E_g and χ are band gap and the electron affinity of the surface, respectively.

Theoretically, the quantitative analysis of the Auger process is feasible if one assumes a constant probability for every electronic transition involved in the electron emission. The resulting formula to calculate SEE coefficient (γ^N) is as follows:[13]

$$\gamma^N = \int_{\max\{E_i-\varepsilon_0,\varepsilon_0\}}^{E_i-2\xi+\varepsilon_0} P_e(\varepsilon)D_c(\varepsilon)T \times\left[\frac{\varepsilon+\varepsilon_0-E_i}{2}\right]d\varepsilon \Bigg/ \int_{\max\{E_i-\varepsilon_0,\varepsilon_c\}}^{E_i-2\xi+\varepsilon_0} D_c(\varepsilon)T \times\left[\frac{\varepsilon+\varepsilon_0-E_i}{2}\right]d\varepsilon, \tag{2}$$

where ε_0 and ε_c are the vacuum level and conduction minimum measured from the valence bottom, ξ is the work function, and $D_c(\varepsilon)$ is the density of states for conduction bands. P_e and T are functions to describe escape probability and Auger transformation of the density of states, respectively. P_e is given as follows:

$$P_e(\varepsilon) = \frac{1}{2}\left[1-\left(\frac{\varepsilon_0}{\varepsilon}\right)^{\beta}\right]^{\alpha}, \tag{3}$$

where α and β are adjustable parameters. We use $\alpha=0.248$ and $\beta=1.0$ from Ref. 11. On the other hand, the Auger transform is given below:

$$T\left[\frac{\varepsilon+\varepsilon_0-E_i}{2}\right] = \int_0^{\varepsilon_v}\int_0^{\varepsilon_v} D_v(\varepsilon_1)D_v(\varepsilon_2) \times\delta(\varepsilon-\varepsilon_1-\varepsilon_2+\varepsilon_0-E_i)d\varepsilon_1 d\varepsilon_2, \tag{4}$$

where ε_v and $D_v(\varepsilon)$ are the valence top and density of states for conduction bands, respectively. The delta function in Eq. (4) allows for electronic transitions that satisfy the energy conservation. So far, theoretical modeling to calculate γ^N usually assumed simplified, bulklike band structures.[11,13,14] However, the Auger neutralization is a surface-specific process and therefore sensitive to surface conditions. In order to describe the surface properties realistically, we obtain ε_0, ξ, $D_v(\varepsilon)$, and $D_c(\varepsilon)$ from the first-principles calculation. This approach allows for investigating effects of various surface conditions on SEE coefficients. In evaluating γ^N, the band gap is an essential parameter. However, it is well known that the local density approximation underestimates the energy gap by 30%–40%. In order to overcome this limitation, we refer to GW results in Ref. 15 and correct the energy gap by shifting valence and conduction bands rigidly by −2.4 eV and +0.5 eV, respectively.

B. Kinetic emission mechanism

In the kinetic emission, the conversion of kinetic energies of incoming ions to the electronic transition is responsible for the electron emission. Experimentally, this mechanism is evidenced in the following observations: The SEE coefficient increases as the incident energy of ion increases.[8,12,16] Within the potential emission mechanism, the velocity of the ion could shift neutralization points above the surface. The interaction with image charges within dielectrics then changes the energy transfer by up to 1 eV. However, this is not enough to explain a large variation of SEE coefficients found in the literature. In addition, the energy distributions of emitted electrons are similar for various ion types, which is not explained by potential emission mechanism.[12] Therefore, it is likely that the kinetic energy plays a direct role in increasing the SEE coefficient. In the case of metallic surfaces, the kinetic emission is observed with ions with large kinetic energies typically of the order of keV. By contrast, insulating surfaces begin to show signatures of kinetic emission at much lower energies below 100 eV.[8,12,16] This implies that the emission mechanism of the insulating surface due to slow ions is fundamentally different from the case for metallic surfaces. In Ref. 12, it was suggested that the electronic excitation into the surface exciton can account for the kinetic emission. However, a microscopic explanation is still in demand.

III. COMPUTATIONAL SETUP

The electronic structures of various MgO surfaces at the optimized geometries are calculated with first-principles density functional calculations using a plane-wave basis set. We use the Vienna Ab-initio Simulation Package (VASP) throughout this work.[17] The ionic potentials are described by projector-augmented-wave method[18] and the exchange-correlation energy of the electrons is described within a generalized gradient approximation.[19] The energy cutoff of 400 eV is used to generate a plane wave basis set. For the k-point integration, we use a $4\times4\times4$ mesh for the cubic unit cell of bulk MgO and equivalent densities of mesh points for various surface models. The atomic coordinates are relaxed until the Hellmann-Feynman forces for each atom are reduced to within 0.02 eV/Å. The vacuum length is set to 10 Å. The lattice constant of bulk MgO is computed to be 4.238 Å in comparison with experimental value of 4.211 Å. The number of layers (6–8) in the surface model is chosen so as to recover the bulk property in the middle layer. To obtain the vacuum level from the first-principles calculation, the potentials are averaged over the plane normal to surfaces and the vacuum level is set to the potential value in the middle of the vacuum.

We try to address the kinetic emission by performing first-principles molecular dynamics simulation (FPMD) for the collision between the ion and MgO surface. The computational framework and parameters are similar to those used

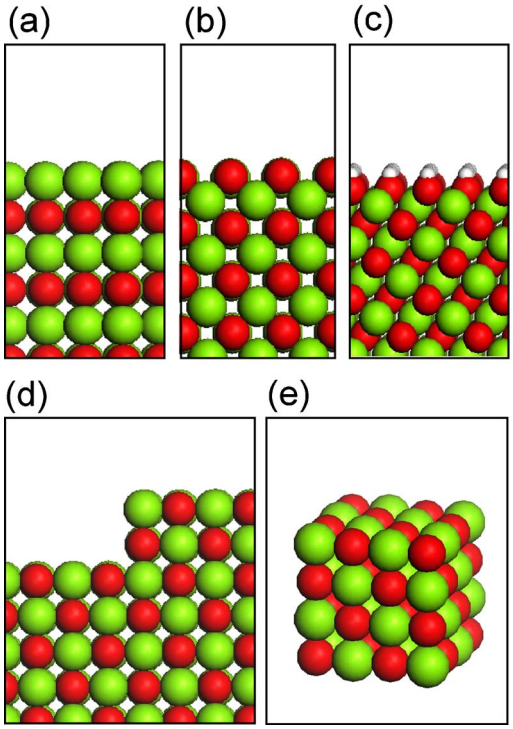

FIG. 1. (Color online) Atomic geometry of various model systems. (a) (100) surface, (b) (110) surface, (c) (111)-OH surface, (d) surface step, and (e) nanocube. The light and dark spheres indicate Mg and O atoms, respectively. The hydrogen atoms in (c) are denoted by small spheres.

in the static electronic-structure calculation as detailed in the above. Since the ions are mostly neutralized just before collision events (~3 Å above the surface), we calculate with neutral atoms incident on the surface. The molecular dynamics is carried out within the microcanonical ensemble, i.e., along the constant-energy trajectory. The time step is set to 1 fs and the total energy is conserved within 3 meV/atom during the total simulation time of 200 fs. The (100) slab models with six layers are used with $2\sqrt{2}\times 2\sqrt{2}$ periodicity along the lateral directions. The bottom layer of the slab is fixed to prevent the drift of model systems.

IV. RESULTS AND DISCUSSION

A. Potential emission properties of various types of surfaces

We first examine the dependence of SEE coefficients (γ^N) on the surface direction by performing calculations on the (100), (110), and (111) surfaces, the main low-index surfaces of rocksalt structures. [See Figs. 1(a)–1(c).] These are also growth directions frequently observed for MgO protective layer. The bulk-terminated (111) surface is polar and electrically unstable. We passivate the oxygen-terminated (111) surface by attaching a hydrogen atom on top of each oxygen atom. The hydrogenated (111)-(1×1) surface[(111)-OH, hereafter] was reported to be more stable than the (100) surface.[20] The computed band structure of each surface is shown in Figs. 2(a)–2(c). Compared to the bulk, new states develop below the conduction bands. The inspection of the squared wave function indicates that these states are distributed outside the MgO surface and extend as much as 6 Å.

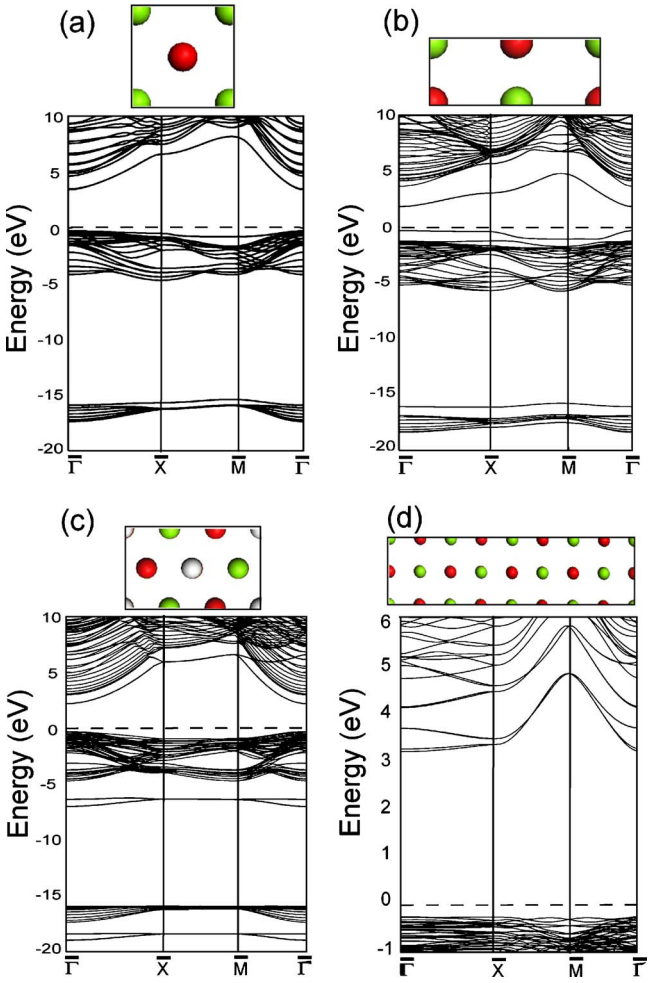

FIG. 2. Band structures of various surface models. (a) (100) surface. (b) (110) surface. (c) (111)-OH surface. (d) Surface step. For each band structure, top views of surface unit cells are also shown on top of each figure. The Fermi level is set to zero (horizontal dashed lines).

This state lies just below the vacuum level and is usually known as an image state. The presence of image states for a MgO surface was also reported in the GW calculation,[15] although the energy level in our results is slightly downshifted compared to the GW estimation. Since these states are bound at the surface, it has small but adverse effects on the SEE coefficients by increasing the denominator in Eq. (2). The work functions, which are set to the relative position of the valence top from the vacuum, are shown in Table I for (100),

TABLE I. Computed SEE coefficients for Auger neutralization process. The work functions are given by the energy difference between the highest occupied state and the vacuum. The band gap is corrected by the scissor operation. The ionization energies in eV are given in the parentheses of each noble gas.

	(100)	(110)	(111)	Step	Cube	*F* center	*V* center
Work function (eV)	7.485	6.886	5.715	7.560	6.797	5.349	7.869
He (24.58)	0.379	0.371	0.412	0.377	0.385	0.368	0.373
Ne (21.56)	0.340	0.323	0.393	0.334	0.343	0.317	0.328
Ar (15.76)	0.174	0.096	0.328	0.163	0.199	0.110	0.129
Kr (14.00)	0.0	0.0	0.166	0.0	0.004	0.043	0.0
Xe (12.13)	0.0	0.0	0.008	0.0	0.0	0.257	0.0

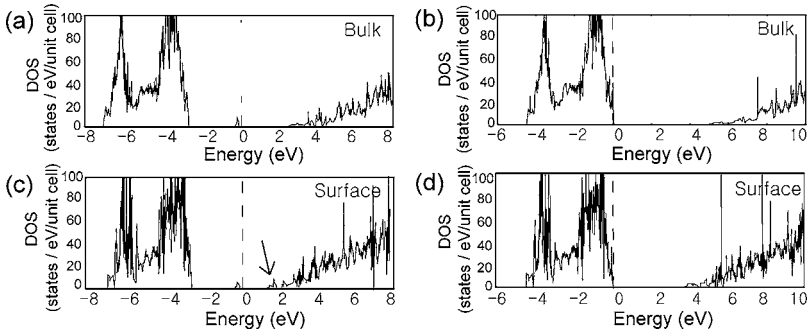

FIG. 3. Density of states (DOS) for *F* and *V* centers in the bulk or on the (100) surface. (a) and (c) are DOS's for *F* center and (b) and (d) are those for *V* center. The Fermi level is set to zero (vertical dashed lines). An arrow in (c) indicates localized surface states developed below the conduction band.

(110), and (111)-OH surfaces. The charge transfer between oxygen and hydrogen atoms forms effective dipole layers between (111)-OH and the vacuum and reduces the work function of the (111)-OH surface substantially.

The SEE coefficients (γ^N) are calculated by evaluating Eq. (2) with density of states and work functions obtained from first-principles calculations. As mentioned in the above, the underestimate of the energy gap is corrected with reference to GW data for (100) surface. We assume that the scissor operation can be uniformly applied irrespective of the surface direction and shift valence and conduction bands with equal amounts to those for the (100) direction. The computational results for γ^N for the representative surfaces with various noble gases are compiled in Table I. First, it is found that γ^N increases monotonically with the ionization energy. The larger ionization energy facilitates transitions into higher energy above the vacuum and results in enhanced SEE coefficients. This is in accordance with the experimental reports and other theoretical estimates.[13] Regarding the orientation of surfaces, SEE coefficients are found to increase in the following order: (110)<(100)<(111)-OH. The largest γ^N for (111)-OH can be explained on the basis of the reduced work function. On the other hand, the larger density of image states for the (110) surface below the vacuum level explains the smallest SEE coefficients. The dependence of γ^N on the surface direction agrees well with experimental results.[5,8] However, it should be noted that surfaces in experiments are frequently terminated with (100) micro-facets and precise comparison should be accompanied with the analysis on the surface morphology.

Next, we examine the effect of topological defects on SEE coefficients. Compared to bulk MgO, new absorption peaks have been observed for MgO surfaces by high-resolution electron energy loss spectroscopy and the diffuse reflectance spectroscopy.[21,22] The *ab initio* Hartree-Folk calculations showed that these peaks originated from the topological defects of surfaces such as steps, kinks, and corners.[23] In Fig. 1(d), a model geometry imitating a MgO (100) surface including a step structure is shown and the computed band structure is given in Fig. 2(d). The flat bands are noticeable in conduction bands due to the localized states that originated from the step edge. Steps with different depths are also computed but the band structures are very similar to that of the double steps in Fig. 2(d). The calculated γ^N for the step model is shown in Table I. Since the work function and electronic structure are close to those of the clean (100) surface, γ^N is almost identical to the values for the (100) surface. In addition to the step, various types of corners are also important topological defects on the MgO surface. Including corner defects increases the size of the supercell significantly. Instead, we calculate on a nano-sized MgO cluster with 64 atoms (32 anions and 32 cations), which includes corners as well as edges. [See Fig. 1(e).] We find that states localized at the corner site appear ~2 eV above the valence top. However, its impact on the SEE coefficient is negligible as shown in Table I.

B. Potential emission properties of surfaces with vacancies

The presence of point defects in MgO has been known to result in a variety of optical, catalytic, and electrical phenomena.[24] The structural and electronic characterizations of these defects are detrimental to understanding material properties of MgO. So far, little is known about the correlation between the vacancy defects and SEE from MgO surfaces. The point defects such as *F* centers (oxygen vacancies) and *V* centers (magnesium vacancies) can be included within the material during the deposition process or generated during the aging process used in activating the discharge cell. In fact, recent experimental results show that the existence of *F* centers in MgO decreases firing voltage.[25] A theoretical model was introduced to explain these results, assuming simplified electronic structures.[14] Based on the first-principles approaches, we study the effects of representative point vacancy defects on the electronic properties and SEE characteristics of MgO.

The vacancies are created on (100) surfaces with the lateral periodicity of 3×3. The atoms are removed symmetrically from both sides of the slab to keep the averaged potential flat in the vacuum region. The computed DOS are shown in Fig. 3. For comparison, the DOS for the bulk model including vacancies are also displayed. The *F* center energies are 2.4 and 2.2 eV from the valence top for the bulk and the surface, respectively. These values are in good agreement with previous computational results.[26] In the case of *V* center, no defect levels are identified within the energy gap. Instead, the Mg vacancy induces delocalized hole states near the valence top. For *F* centers, localized bands are found just below the conduction bottom [see an arrow in Fig. 3(c)]. These states originated from the image states and can be conceived as perturbed states due to changes in electrostatic potentials near the defect sites.

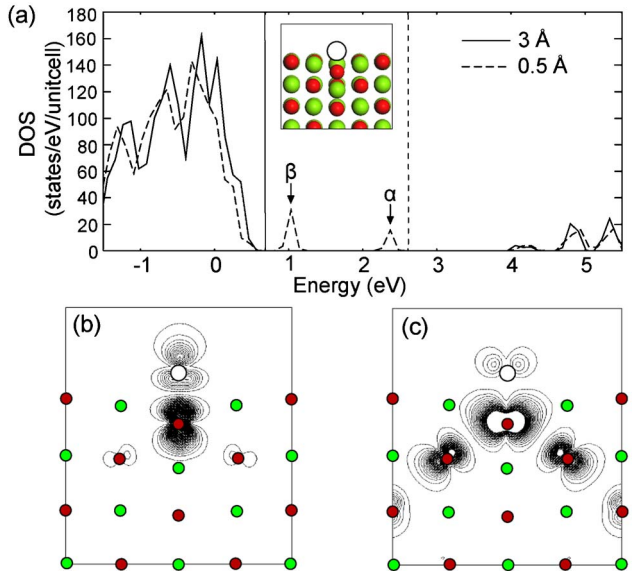

FIG. 4. (Color online) (a) Density of states when the Ar atom is above the surface by 3 or 0.5 Å. The Fermi level is indicated by vertical lines. The localized states (α and β) are indicated by vertical arrows. The inset shows the relaxed geometry when the Ar-surface distance is 0.5 Å. Note that the O atom below the Ar atom is relaxed downward substantially. (b), (c): Contour plots of α and β states in (a), respectively. Light and dark grays indicate Mg and O atoms, respectively. The Ar atom is denoted by empty circles.

The computed γ^N values for the surface with point defects are listed in Table I. We find that the V center has little influence on the SEE characteristics, which is reasonable because the work function and DOS are very similar to those for the clean surface. The slight decreases are attributed to the larger work function. On the other hand, the F center substantially affects SEE for ions with small ionization energies, such as Kr and Xe atoms. Note that these ions do not contribute to SEE by Auger neutralization process for perfect (100) surfaces. The mid-gap states associated with the F center enable the electrons to excite above the vacuum level. These results are good in comparison with previous results.[14,25]

C. Kinetic emission—basic principle

Before carrying out full-scale FPMD simulations, we examine how the electronic structure is affected as an atom approaches to the MgO surface. For this, we perform static calculations with various distances between an ion (an Ar atom in this case) and the surface. The positions of Ar atoms and ions in the bottom layer of the MgO slab are fixed while all other atoms are relaxed. The inset in Fig. 4(a) shows relaxed geometries when the Ar atom is above the surface by 0.5 Å. Laterally, the Ar atom is on top of the oxygen atom in the top layer. The relaxed distance between O and Ar atoms is 1.3 Å. The DOS in Fig. 4(a) shows the electronic structures for two different ion-surface separations. When the Ar atom is close to the surface, new states (indicated as α and β) are created within the band gap. The contour plots of these states are shown in Figs. 4(b) and 4(c). It can be found that the α state originated from the antibonding between Ar-p and O-p orbitals. On the other hand, the β state is composed of mainly p orbitals of oxygen atoms in the first and second layers that are close in distance. The antibonding character can be also confirmed from the nodal structures in between atomic orbitals. With the new localized state fully occupied, the Fermi level rises into the energy gap of MgO. Further approach of the ion to the surface causes the localized state to climb over the conduction bottom and eventually reach the vacuum level. This will lead to a finite probability of those states jumping into the vacuum, hence the secondary electron emission. (Note that the emission process is beyond the adiabatic approximation employed in this work and the rise of the Fermi level stops near the conduction bottom.) The emission into the vacuum state is facilitated by the negative electron affinity of the MgO (100) surface. On the other hand, when the Ar atom is pushed on top of the Mg atom, we do not identify any state developed within the energy gap.

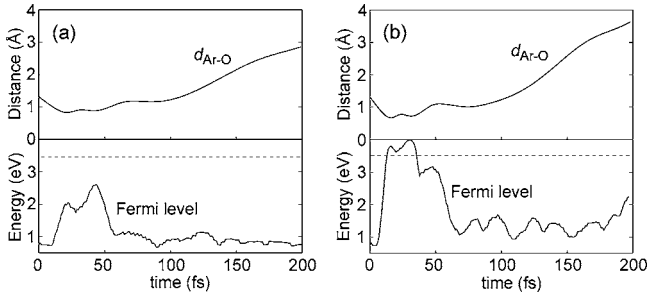

FIG. 5. Changes of the Fermi level and distances between Ar and O atoms (d_{Ar-O}) during the molecular dynamics simulations when Ar atoms impinge on the (100) surface with initial kinetic energies of (a) 10 eV and (b) 30 eV. The conduction bottom is indicated by horizontal dashed lines.

Next, we carry out FPMD simulation on the Ar atom colliding vertically with the oxygen atom in the MgO surface with kinetic energies of 10 or 30 eV. In Fig. 5, the distance between Ar and O atoms, and the position of the Fermi level are plotted as a function of time. With higher kinetic energies, the Ar atom penetrates deeper into the surface. In addition, the Fermi level shifts up toward the conduction band as found in the above static simulations. The electron emission could occur when the defect levels are above the vacuum level. It is noticeable that the Fermi level briefly touches the conduction bottom at a kinetic energy of 30 eV [see Fig. 5(b)]. Since the conduction bottom is close to the vacuum level, the threshold energy for kinetic emission would be close to this value. It is beyond the scope of this work to obtain SEE coefficients directly from FPMD simulations. Instead, we define the " 'excitation' time" (τ_{ex}) as a working parameter by integrating total time during which the Fermi level is above the conduction bottom. We assume that τ_{ex} correlates well with the escape probability of the electron and compare τ_{ex} for various conditions in the next section.

D. Kinetic emission properties—parameter dependence

In order to study how the kinetic electron emission depends on the ion species and incident directions, we perform FPMD simulations with various conditions of incoming noble gases, such as atomic species, impact points on MgO, incident energies, and collision angles. We choose Ne and Xe

TABLE II. Computed excitation time in femtoseconds with respect to kinetic energies, directions, and species of incident ions.

Energy (eV)	Direction	Ne	Xe
30	$\langle 00\bar{1}\rangle$	4	15.8
50	$\langle 00\bar{1}\rangle$	6.25	28.3
100	$\langle 00\bar{1}\rangle$	4.75	28.63
100	$\langle \bar{1}\bar{1}\bar{1}\rangle$	8.25	25.63

atoms for the detailed investigation because they constitute primary plasma gases in PDP cells. The impact points are selected on 4×4 uniform grids on $\sqrt{2}\times\sqrt{2}$ unit cell of (100) surface, and the incoming direction is set to $\langle 00\bar{1}\rangle$ or $\langle \bar{1}\bar{1}\bar{1}\rangle$. This is to simulate ions colliding on surfaces with the growth direction of (100) and (111), respectively; in the discharge cell, most ions arrive at the MgO surface from the normal direction. Since the (111)-textured surface is usually faceted with (100) surfaces in a triangular pyramid, the normal incidences on those surfaces are equivalent to a collision on a (100) surface with the angle of $\pi-\arctan(\sqrt{2})$ (in radians) from the surface normal vector. We choose $\langle \bar{1}\bar{1}\bar{1}\rangle$ as a representative direction. The distributions of kinetic energies of ions were estimated by Monte Carlo simulations,[27,28] and they exhibit exponential decays with respect to the kinetic energy. Considering that the SEE coefficient scales almost linearly with the kinetic energy, ions with kinetic energies of 30–60 eV will play a dominant role in the kinetic emission.

We perform FPMD simulations for the time interval of 200 fs, which turn out to be enough to measure τ_{ex} up to the kinetic energy of 100 eV. The τ_{ex}'s averaged over impact points are compiled in Table II. Several key features merit discussions: (i) It is noticeable that Xe, which does not contribute to SEE by Auger neutralization, is able to produce secondary electrons through the kinetic emission mechanism. This is an interesting observation because a PDP cell typically operates with Ne-Xe gas mixtures. In addition, the surface of MgO is exposed to continuous collisions with Xe atoms with the mean kinetic energy bigger than that of Ne atoms.[27,28] (ii) Even though Ne atoms would efficiently transfer energies to oxygen atoms owing to the similar atomic mass, τ_{ex} is higher for Xe atoms. This is due to the much larger ionic mass of Xe atoms, which allows for longer collision times. (iii) For Ne atom, the $\langle \bar{1}\bar{1}\bar{1}\rangle$ direction is more efficient than the $\langle 00\bar{1}\rangle$ direction to extend τ_{ex}. The impacts along the $\langle \bar{1}\bar{1}\bar{1}\rangle$ direction efficiently induce subsequent collisions between oxygen atoms. This promotes the electronic excitation through the antibonding between oxygen p orbitals (see the previous section) and therefore leads to prolonged τ_{ex}. On the other hand, the collision with Xe atoms is less sensitive to the direction, which is understandable considering the larger atomic radius of Xe atoms (1.24 Å) compared to that of Ne atoms (0.51 Å).

V. SUMMARY

In summary, we have introduced first-principles methods to investigate secondary electron emission properties of MgO surface used as a protective layer in PDP. The surface-dependent electronic structures and work functions were obtained from the density functional calculations. The SEE coefficients depending on the surface direction are in good comparison with experimental observations. The (111)-OH surface was found to enhance SEE coefficients for all noble gases owing to the surface dipole lowering the work function. The presence of point defects such as F centers on the surface enabled the SEE by Kr and Xe atoms. The kinetic emission mechanism, on the other hand, was addressed using the molecular dynamics simulation within the adiabatic approximation. Although the emission process itself was not described by the present computational approaches, the excitations of energy levels were identified, which would account for the main procedure leading to kinetic electron emission by slow ions. The most interesting observation would be a possible contribution of Xe atoms to the electron emission through the collision effects. This will be useful information for designing gas mixtures used in PDP.

ACKNOWLEDGMENTS

This work was supported by Samsung SDI and the Korea Science and Engineering Foundation through the Basic Research program (Grant No. R01-2006-000-10883-0). EC and TK appreciate financial supports by second BK21 project. The computations were carried out at Korea Institute of Science and Technology Information (KISTI) through Seventh Strategic Supercomputing Program.

[1] M. Yoo, E. Hwang, H. Shin, D. Lee, and Y. Cho, *SID Digest* (Tech. Dig. Society for Information Display, 2005), p. 1836.
[2] J. P. Boeuf, J. Phys. D **36**, R53 (2003), and references therein.
[3] T. J. Vink, A. R. Balkenende, R. G. F. A. Verbeek, H. A. M. van Hal, and S. T. de Zwart, Appl. Phys. Lett. **80**, 2216 (2002).
[4] H. Uchiike, K. Miura, N. Nakayama, T. Shinoda, and Y. Fukushima, IEEE Trans. Electron Devices **23**, 1211 (1976).
[5] V. van Elsbergen, P. K. Bachmann, and G. Zhong, Proceedings of the 7th International Display Workshops, IDW '00, Sendai, Japan (2000), p. 687.
[6] S. Y. Park, M. J. Lee, H. J. Kim, S. H. Moon, S. G. Kim, and J. K. Kim, J. Vac. Sci. Technol. A **23**, 1162 (2005).
[7] Y. H. Cheng, H. Kupfer, and F. Richter, J. Appl. Phys. **94**, 3624 (2003).
[8] E. H. Choi, J. Y. Lim, Y. G. Kim, J. J. Ko, D. I. Kim, C. W. Lee, and G. S. Cho, J. Appl. Phys. **86**, 6525 (1999).
[9] A. Miyamoto, R. Endou, H. Kikuchi, H. Tsuboi, M. Koyama, A. Endou, M. Kubo, C. A. Del Carpio, and H. Kajiyama, Proceedings of the 12th International Display Workshops, IDW'05, Sendai, Japan (2005), p. 423.
[10] A. von Engel, *Ionized Gases* (AIP, New York, 1994).
[11] H. D. Hagstrum, Phys. Rev. **122**, 83 (1961).
[12] P. Riccardi, M. Ishimoto, P. Barone, and R. A. Baragiola, Surf. Sci. **571**, L305 (2004).
[13] Y. Motoyama, H. Matsuzaki, and H. Murakami, IEEE Trans. Electron Devices **48**, 1568 (2001).
[14] Y. Motoyama and F. Sato, IEEE Trans. Plasma Sci. **34**, 336 (2006).
[15] M. Rohlfing, N.-P. Wang, P. Krüger, and J. Pollmann, Phys. Rev. Lett. **91**, 256802 (2003).
[16] S. K. Lee, J. H. Kim, J. Lee, and K.-W. Whang, Thin Solid Films **435**, 69 (2003).
[17] G. Kresse and J. Hafner, Phys. Rev. B **47**, 558(R) (1993); **49**, 14251 (1994).
[18] P. E. Blöchl, Phys. Rev. B **50**, 17953 (1994).
[19] J. P. Perdew, K. Burke, and M. Ernzerhof, Phys. Rev. Lett. **77**, 3865 (1996).
[20] V. K. Lazarov, R. Plass, H.-C. Poon, D. K. Saldin, M. Weinert, S. A. Chambers, and M. Gajardziska-Josifovska, Phys. Rev. B **71**, 115434 (2005).

[21]J. S. Ferrer, J. M. Rojo, M. Salmeron, and G. A. Somorjai, Philos. Mag. A **45**, 261 (1982).
[22]S. Coluccia, A. Barton, and A. J. Tench, J. Chem. Soc., Faraday Trans. 1 **77**, 2203 (1981).
[23]A. L. Shluger, P. V. Sushko, and L. N. Kantorovich, Phys. Rev. B **59**, 2417 (1999).
[24]A. Gibson, R. Haydock, and J. P. LaFemina, Phys. Rev. B **50**, 2582 (1994).
[25]Y. Motoyama, Y. Hirano, K. Ishii, Y. Murakami, and F. Sato, J. Appl. Phys. **95**, 8419 (2004).
[26]L. N. Kantorovich, J. M. Holender, and M. J. Gillan, Surf. Sci. **343**, 221 (1995).
[27]S. J. Yoon and I. Lee, J. Appl. Phys. **91**, 2487 (2002).
[28]L. C. Pitchford, J. Wang, D. Piscitelli, and J. P. Boeuf, IEEE Trans. Plasma Sci. **34**, 351 (2006).